Biogeochemical cycling of manganese and iron in a macrotidal and hyperturbid estuary subject to flow-driven sedimentation

Mohammed Barhdadi, Aurélia Mouret, Christine Barras, Sabine Schmidt, Grégoire Maillet, Nour El Imene Boukortt, Meryem Mojtahid, Matthieu Durand, Bruno Deflandre, Corentin Guilhermic, et al.

Biogeochemical cycling of manganese and iron in a macrotidal and hyperturbid estuary subject to flow-driven sedimentation

Mohammed Barhdadi[1,] *, Aurélia Mouret[1], Christine Barras[1], Sabine Schmidt[2], Grégoire M. Maillet[1], Nour El Imene Boukortt[1], Meryem Mojtahid[1], Matthieu Durand[3], Bruno Deflandre[2], Corentin Guilhermic[1], Aubin Thibault de Chanvalon[4], Sylvain Rigaud[5], Eric Bénéteau[1], Edouard Metzger[1]

[1] Univ Angers, Nantes Université, Le Mans Univ, CNRS, UMR 6112, Laboratoire de Planétologie et Géosciences, 49000 Angers, France

[2] Université de Bordeaux, CNRS, Bordeaux INP, UMR 5805 EPOC, France

[3] Ecole supérieure d'agro-développement international. 4, rue Joseph Lakanal. 49000 Angers

[4] Université de Pau et des Pays de l'Adour, E2S UPPA, CNRS, IPREM, Pau, France

[5] Univ. Nîmes, UPR 7352 CHROME, Nîmes, France

*Corresponding author : barhdadi19@gmail.com LPG, Laboratoire de Planétologie et Géosciences, UMR CNRS 6112, Université Angers, 2 Boulevard Lavoisier, FRANCE - 49045 Angers Cedex 1, +33651319213

Abstract

The study of manganese (Mn) and iron (Fe) cycling in early diagenetic processes in estuaries is crucial for understanding the functioning of these vital ecosystems and predicting their responses to environmental change. The present study investigates the dynamic interplay of Mn and Fe in early diagenetic processes at highly contrasted hydrosedimentary conditions in the Loire estuary, which is very rare and allows a comprehensive framework to understand diagenetic processes in a very dynamic environment. One campaign took place in the Brillantes intertidal mudflat in March 2015 (PV1), while 3 others took place in a muddy riverbed along the navigation channel off the city of Paimboeuf during a decennial flood in February (RR1-4), under moderate discharge in June (RRK-4) and low in August 2021 (RR2-4). The monitored riverbed station was upstream, under and downstream the maximum turbidity zone, respectively. By combining sequential extraction techniques for Mn and Fe in solid phases and pore-water analysis, the study provides insights into the behaviour of these elements in sedimentary environments and reveals their speciation and association with specific mineral phases and forms during different diagenesis stages. The remobilization of Mn and Fe in the surface sediments of the Brillantes mudflat (PV1) allows iron sulphide formation within the upper 50 cm of the sediment column (above the sulphate penetration depth). The deeper layers show other authigenic phases formation, such as the probable precipitation of vivianite below the sulphate depletion depth and progressive precipitation of carbonate at depth, leading to definitive burial and accumulation. At the muddy riverbed, following the exceptional flood in February 2021 (RR1-4), significant sediment erosion occurred unveiling to the water column old and reduced sediments. Sharp pore-water gradients for dissolved Mn, Fe and sulphate indicated the sudden exposure of the old ^{7}Be-free and anoxic sediment to low-salinity, well-oxygenated water. Despite its dark colour, this sediment showed no authigenic FeS/FeS_2 phases. Four months later, changes in the estuarine environment (low river discharge) and the presence of a maximum turbidity zone (TMZ) led to a new deposition of a sediment layer (RRK-4) triggering transient diagenetic reactions. The freshly deposited sediment layer developed important recycling of dissolved Mn, Fe and sulphate above the precedent sediment water interface (SWI) generating a double peak, accompanied by consistently low concentrations of solid Mn and Fe phases specially FeS/FeS_2 and Mn bound to FeS/FeS_2 compared to PV1. Six months after the flood event, in August (RR2-4), the discernible attenuation of dissolved Mn and Fe peaks and sulphate concentration, indicated a gradual recovery of characteristic sediment profiles with the well-known redox layer succession. Overall, despite important sulphate reduction within

sediments from both the river and its adjacent mudflats, pyritization is not a major process for Mn and Fe burial. The intense hydrodynamics of the mid estuary prevents thermodynamical equilibrium between pore-water chemistry and solid phases not allowing pyrite formation while in the calmer conditions of intertidal mudflats, pyrite accumulates in intermediate depths but carbonates and phosphates seem to be the preferential phases of burial probably related to methane production and phosphate availability.

Keywords: Loire, speciation, diagenesis, transient state, sedimentation, disturbance.

1. Introduction

Estuaries are unique and dynamic systems formed at the meeting point of freshwater rivers or streams and saline marine waters and are subject to the influence of tidal and fluvial processes (Perillo, 1995). Most macrotidal estuaries have a region of elevated suspended sediment concentrations called the estuarine turbidity maximum zone (TMZ) (Ciffroy et al., 2003). The TMZ is usually located near the landward end of the salinity intrusion (Woodruff et al., 2001). Different hydrodynamic processes can support the TMZ such as the increase in tidal range (hypersynchronous estuary), which is favoured by the convergence/roughness ratio of the shore (Allen et al., 1980). In macrotidal estuaries, fluctuations in tidal cycles and shifts in freshwater discharge may alter the position of the TMZ along the estuarine axis and change sediment deposition patterns (Jalón-Rojas et al., 2016; Migniot, 1972). These variations result in a seasonal shift of the sediment accumulation zone, affecting the transport and cycling of a variety of biogeochemical elements, including essential micronutrients such as manganese (Mn) and iron (Fe) (Morris et al., 1982).

Mn and Fe are key elements for living organisms (Burdige, 1993; Raven, 1990). Thanks to their redox properties, in particular in sediment, they can serve as important alternative oxidants for carbon degradation (Thamdrup and Dalsgaard, 2000; Vandieken et al., 2006). In estuaries, the interplay between the release of Mn and Fe into the pore-water or the water column then their reincorporation and storage in the solid phase influence their availability and persistence in the sediments. Under conditions where sediments are low in oxygen and with low sulphide concentrations, Fe(II) and Mn(II) can be released into the water column as the formation of insoluble compounds such as FeSx, which would trap these metals, is avoided (Wytze K. Lenstra et al., 2021; Scholz et al., 2014). Conversely, Fe(III) and Mn(IV) tend to precipitate under oxidizing conditions (Froelich et al., 1979). The reactivity of Mn and Fe may influence the behaviour of many other elements. For example, Mn and Fe oxides strongly adsorb trace metals (Shaw et al., 1990). Additionally, Fe oxides can adsorb and

sequester phosphorus, limiting its bioavailability (Anschutz et al., 1998; Pant and Reddy, 2001), while Mn affects nitrogen dynamics through interactions with organic matter and microbial processes (Luther et al., 1997). Finally, authigenic precipitation of the reduced metals with carbonates, sulphides, or phosphate anions and subsequent solid phase equilibrium can control their respective cycles (Mehner, 2009).

While early diagenesis in marine sediments is often described as a steady-state process (Berner, 1980), the geochemical composition of the sediments evolves through transient states. These changes can be attributed to factors such as changes in organic carbon input, oxygen content, sedimentation rates, and local biological activity (Sundby, 2006). Numerous studies have highlighted how changing environmental conditions affect transient diagenesis. Rozan et al. (2002) described the conversion of reactive Fe oxides to the FeS/FeS_2 in a shallow coastal bay and attributed it to sulphate reduction increasing with temperature while Saulnier and Mucci (2000) demonstrated that the release of Mn in pore-water seems to be mainly controlled by the dissolution of Mn-carbonate or a mixed Mn–Ca-carbonate. Phenomena leading to transient states can occur at different temporal and spatial scales. In continental margins, significant disruptions can occur due to remobilization of bottom sediments during flood events (Deflandre et al., 2002; Mucci et al., 2003; Mucci and Edenborn, 1992; Pastor et al., 2018; Sundby, 2006). In estuaries, bed reworking, sediment transport and deposition, especially during extreme flood events, may have a significant impact on diagenetic processes and the associated benthic community (Hulot et al., 2023). This is evident as several decimetres of sediment can be rapidly suspended and deposited instantaneously (Hulot et al., 2023; Pastor et al., 2018). In estuarine intertidal mudflats, flood events combined to strong winds can affect the Fe and Mn cycles through the combination of resuspension/deposition of a freshly transported material from the watershed that is rich in metallic oxides (Thibault de Chanvalon et al., 2016). After deposition, the classical vertical diagenetic series is gradually restored by successive release of dissolved Mn and Fe towards pore-water over a period of few weeks until reaching steady state during summer (Thibault de Chanvalon et al., 2016). As the sediment becomes compact and the microphytobenthos biofilm develops, macrofauna increase biological reworking drastically enhancing metal benthic effluxes and potentially limiting their burial as authigenic sulfidic phases (Thibault de Chanvalon et al., 2017).

Given the complexity of Mn and Fe cycling processes after sediment deposition, the aim of this study is to investigate the burial and recycling of Mn and Fe in the middle Loire estuary, focusing on two contrasting hydrodynamic environments: a muddy riverbed near the

navigation channel and an adjacent large intertidal mudflat. We hypothesize that extreme hydrodynamic events, such as the exceptional flood in February 2021 and the TMZ shift, significantly affect the geochemical behaviour of Mn and Fe and deviate from traditional diagenetic steady-state models. These events are likely to shift redox conditions, altering the geochemical profiles of the metals and affecting their interaction at the sediment-water interface. The application of sequential extraction allows a detailed investigation of Mn and Fe speciation in the different sediment layers and provides insights into their dynamic behaviour during and after sediment deposition, which is influenced by extreme hydrological conditions. In addition, the integration of pore-water chemistry and radionuclide profiles, such as ^{210P}b and ^{7}Be, provides a unique temporal resolution that captures short-term changes and the long-term effects of these events on the metal cycle in the land-sea continuum.

2. Material and methods

2.1. Study site

The Loire River is the longest river in France (1012 km), draining a watershed of ~ 118,000 km^2, covering one-fifth of metropolitan France. The average annual flow of the Loire River is 900 m^3 s^{-1}, fluctuating between periods of low water in summer and autumn (300 m^3 s^{-1}) and high discharge in winter and spring (>1800 m^3 s^{-1}) (Hydro B, 2021). The Loire estuary extends over 80 km, and covers an area of ~ 217 km^2 and a catchment area of 7470 km^2 (Fig. 1; Ciffroy et al., 2003; OFB, 2017). The limits of the salinity ranges fluctuate daily, monthly and seasonally with hydrological conditions. Based on the average annual discharge and tidal conditions, five areas are defined from the estuary to Nantes (Fig.1; Gallene, 1974): 1) the euhaline zone (salinity = 35–30) from the estuary to Saint-Nazaire, 2) the polyhaline zone (30–18) from Saint-Nazaire to Donges, 3) the mesohaline zone (18–5) from Donges to Cordemais, 4) the oligohaline zone (5–0.5) from Cordemais to Nantes and 5) the freshwater zone (< 0.5) upstream of Nantes. Being macrotidal (tidal range: 3 to 6 m), the estuary is characterised by turbidity maximum zone (TMZ) defined as the region where suspended particles matter (SPM) concentrations exceeds 500 mg L^{-1} (Gallenne, 1974) and extending over 20 km (Migniot, 1993). During periods of low flow, typically in summer, the TMZ tends to shift farther upstream (Jalón-Rojas et al., 2016). This results locally in high SPM concentrations, often reaching several hundred milligrams per litre (Hulot et al., 2023).

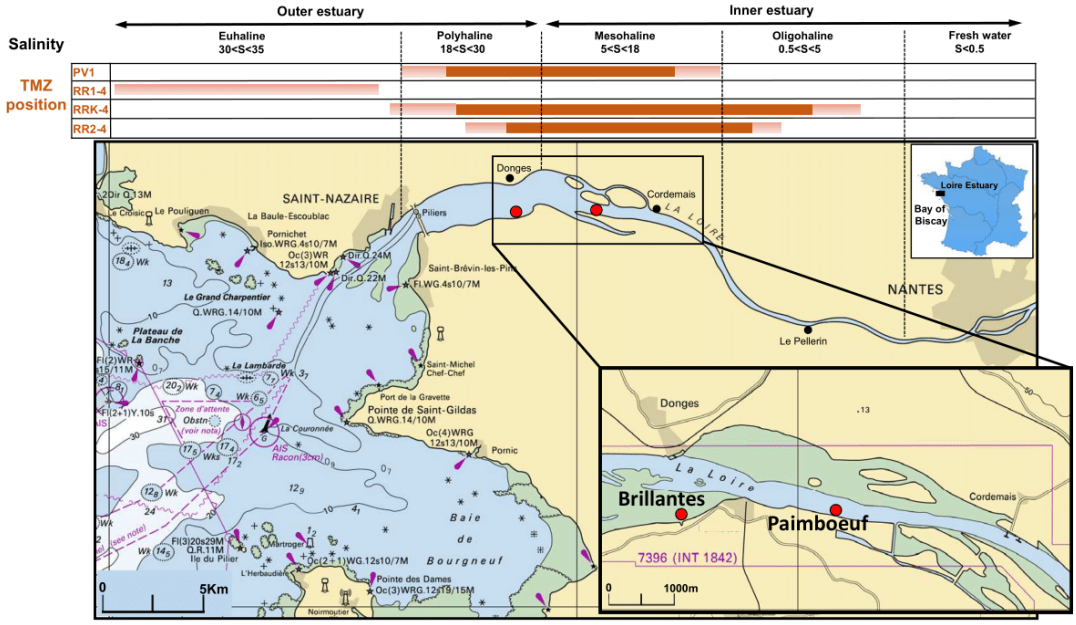

Fig1. Map of the Loire estuarine zone with morphological subdivisions of the estuary, salinity domains under annual averaged flow conditions (after Gallene, 1974) and the position of the turbidity maximum zone (dark orange) and its extension (light orange) during each campaign (after GIP Loire, 2023). Red circles represent the sampling sites (the muddy riverbed station at Paimboeuf and the Brillantes intertidal mudflat). Bathymetric maps are sourced from DATA.SHOM (2024).

2.2. Sampling

The first site is located on the unvegetated part of the Brillantes intertidal mudflat (largest mudflat of the Loire estuary; ~1350 ha) about 150 m from the shoreline (47°16′59.05″N; 2°3′47.63″W; Fig.1) and was sampled in March 2015 (PV1) when the water discharge was about 950 m^3 s^{-1}. The second one is located on the left subtidal bank of the inner Loire estuary at Paimboeuf (47°17'12.2"N 1°59'46.2"W; depth range 5 to 10 m; Fig.1), 7 km upstream of the Brillantes mudflat and was sampled three times during REBELRED cruises in 2021 (Metzger and Maillet, 2021): (1) in February (RR1-4) when the Loire experienced an exceptional flood event with a peak discharge up to 4300 m^3 s^{-1} that expelled the TMZ beyond the western limit of the Fig.1 map as a plume, after intense rainfall episodes (Fig.2), (2) in June (RRK-4) with a water discharge around 384 m^3 s^{-1} and, (3) in August (RR2-4) when the water discharge dropped to 231 m^3 s^{-1} (Fig.2) and the TMZ was centred on the sampling zone. During sampling at Paimboeuf station, bottom salinity varied from 0.1 in February to 2.5 and 22.9 in June and August respectively.

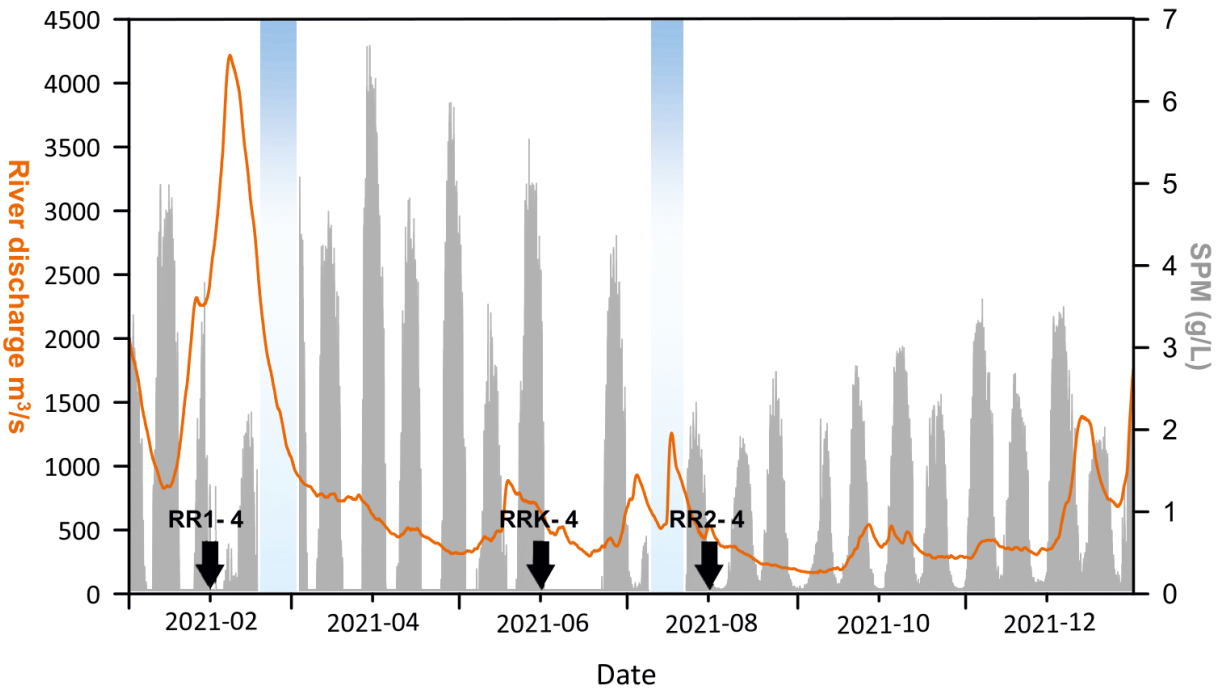

Fig 2. Daily averaged river discharge records at Montjean-sur-Loire gauging station and high frequency records of suspended particulate matter (SPM) in surface waters at Paimboeuf in 2021. Data provided by Hydro B(2021) and SYVEL, (2021). Black arrows indicate different REBELRED sampling campaigns. Blue rectangles indicate periods when SPM data were not available.

At the Brillantes mudflat, two long sediment cores (PV1a: 5.4 m; PV1b: 5.3 m) were recovered using a percussion corer. The core PV1a was collected for sedimentological analyses (grain-size, photography, x-ray imagery and sedimentary columns). To characterize grain-size distribution of the different facies in the cores, samples were selected on the basis of visual description of the sediment core and analysed using a Malvern™ laser diffractometer Mastersizer 3000 laser diffractometer. Photographs were obtained using a NIKON Reflex D5600 camera, lens 35/1.8G, mounted on a photo bench and X-ray imagery was carried out using an X-ray imaging system SCOPIX2 at EPOC (Univ Bordeaux). PV1b was collected to determine the chemical composition of both pore-water and particles. The core was sliced in a N_2 purged glove bag into 2 cm slices every 5 cm for the first meter, and every 10 cm deeper. At the same station, an interface core (PV1b.i: 0.35 m) was sampled by hand using a PVC tube to obtain a well-preserved sediment surface and to avoid the possible loss of surface sediment due to the percussion coring used to obtain the long core. The sediment of this core was also sliced in a N_2 purged glove bag into 2 mm slices for the first 2 cm, 0.5 cm slices from 2 to 5 cm depth, 1 cm slices from 5 to 20 cm depth and 2 cm slices every 5 cm deeper. A fraction of each sampled sediment slice was frozen for porosity and radionuclides determinations and chemical extractions. The rest was centrifuged (15 min at

3500 rpm) and pore-water recovered and filtered through 0.2 µm Minisart® RC25 cellulosic syringe filters and separated into different aliquots for analyses.

At the muddy riverbed station (Paimboeuf), in February, two interface cores were collected using a MC6 Octopus multicorer (RR1-4a.i: 0.4 m; RR1-4b.i: 0.5 m). RR1-4a.i was collected for sedimentological analyses. RR1-4b.i was dedicated to pore-water separation and related analyses. In June, 145 days later, two long sediment cores (RRK-4a: 1.2 m; RRK-4b: 1.8 m) were recovered using a Kullenberg corer. RRK-4a was collected for sedimentological analyses and RRK-4b was collected to determine the chemical composition of both pore-water and solid phase. At the same station, an interface core (RRK-4b.i: 0.35 m) was sampled using a Fantacore multicorer to obtain a well-preserved sediment surface and to avoid the possible loss of surface sediment due to the Kullenberg coring. In August, an interface core was collected, (RR2 -4b.i: 0.45 m) following the same treatment as for RR1. All cores collected during REBELRED cruises were processed using the same slicing and analysis protocol as in the Brillantes mudflat. To simplify the result descriptions, mission names will be used instead of individual core names.

2.3. Porosity and ^{210}Pb and ^{7}Be profiles

The frozen sediment aliquots were freeze-dried and the weight lost during freeze-drying, corrected for the sea salt content, was used to calculate sediment porosity.

Profiles of radionuclides of interest (^{210}Pb, and ^{7}Be) were established on all interface and long sediment cores from the riverbed station. For PV1, ^{7}Be could not be investigated because activity measurements were done too long after sampling and ^{7}Be was no longer detectable. Gamma emitter activities were measured on about 5 g of dry sediment using a Broad Energy Germanium detector BEGe^{TM} (Dubosq et al., 2021). First, rapidly after the cruises due to the rapid decay of ^{7}Be ($T_{1/2}$ = 53 days), the uppermost layers of the interface cores were measured downcore until negligible ^{7}Be activities were reached. Several weeks later, sediment layers were measured to determine ^{210}Pb. Excess ^{210}Pb ($^{210}Pb_{xs}$) was calculated by subtracting the parent isotope ^{226}Ra from the total ^{210}Pb measured in the sediments. Different models could be used to estimate sediment age or accumulation rates (Sanchez-Cabeza and Ruiz-Fernández, 2012). When sedimentation tend to be continuous, the CF:CS (constant flux and constant sedimentation) model is the simplest one to estimate sediment accumulation rates from the exponential decay of $^{210}Pb_{xs}$ with depth. If sedimentation is more erratic and does not satisfy the CF:CS condition, an alternative is to use the CIC (constant initial concentration) model to calculate the age (t, in year) of the sediment layer according to (1):

$$t = \left(\frac{1}{\lambda}\right) \ln\left(\frac{A_0}{A_z}\right) \qquad (1)$$

where A_0 and A_z are the ^{7}Be activities, respectively, at the sediment-water interface (SWI) and at the depth z respectively, and λ is the decay constant (0.0311 yr^{-1}) of ^{210}Pb.

2.4. Pore-water analyses

Pore-water was filtered and an aliquot for total dissolved manganese, iron, sulphur (interpreted as sulphate, after Metzger et al. (2007)), calcium and sodium was acidified with a single drop of ultrapure HNO_3 for less than 5 mL of sample and then diluted 10-fold with a 1% HNO_3 solution for ICP-AES analysis using a Thermo Scientific iCAP 6300 spectrometer with a precision below 2 %. Sulphide was analysed in another interface core from the same multicorer during RR1-4 and RR2-4 cruises. Concentrations were always below the quantification limit (1 µmol L^{-1}, data not shown) using the blue methylene method for pore-waters (Metzger et al., 2007).

2.5. Sequential chemical extractions and analyses

To determine Mn and Fe partitioning in the solid-phase of PV1, RR1-4 and RRK-4, 100 mg of freeze-dried grounded sediment of each sample were subjected to a five-step sequential extraction procedure (Table 1). 10 mL of extractant was used in each step. Sediment was fractionated as followed: (1) ascorbic acid (pH 7.5) to extract poorly ordered Mn oxides and ferrihydrite (Anschutz et al., 2005; Kostka and Luther, 1994; Raiswell et al., 2010; Rennert et al., 2021); (2) 1 M HCl to dissolve Mn and Fe carbonates, reducible crystalline Fe oxides (Chester and Hughes, 1967; Lenstra et al., 2019), mackinawite and vivianite (Kubeneck et al., 2021); (3) citrate buffered dithionite to extract crystalline Mn and Fe oxides (W. K. Lenstra et al., 2021; Poulton and Canfield, 2005); (4) ammonium oxalate to dissolve recalcitrant Mn oxides and magnetite (Phillips and Lovley, 1987; Poulton and Canfield, 2005) and (5) concentrated HNO_3 to extract pyrite (FeS/FeS_2) and Mn bound to pyrite (Lord III, 1982; Claff et al., 2010). The samples were centrifugated and the supernatant was recovered and diluted with 1% HNO_3. Mn and Fe concentrations were analysed using ICP-AES 6300 Thermo-Fischer.

Table 1. Sediment sequential extraction scheme for Mn and Fe and targeted mineral phases.

Step	Extractant	Time (hours)	Terminology	Target phases	References
1	0.17 M sodium citrate, 0.6 M sodium bicarbonate and 0.057 M ascorbic acid (pH 7.5)	24	Mn Asc Fe Asc	Poorly ordered Mn oxides Ferrihydrite	Kotska and Luther, 1994; Anschutz et al., 2005; Raiswell et al., 2010
2	1 M HCl	4	Mn HCl Fe HCl	Mn carbonates, Reducible crystalline Fe oxides, Fe carbonates, Mackinawite and Vivianite	Chester and Hughes,1967; Lenstra et al., 2019; Kubeneck et al., 2021
3	50 g L^{-1} sodium dithionite solution buffered to pH 4.8 with 0.35 M acetic acid/ 0.2 M sodium citrate	4	Mn CDB Fe CDB	Crystalline Mn oxides Crystalline Fe oxides	Poulton and Canfield,2005; Lenstra et al., 2021
4	0.2 M ammonium oxalate/ 0.17 M oxalic acid (pH 3.2)	6	Mn Oxalate Fe Oxalate	Recalcitrant Mn oxides Magnetite	Phillips and Lovley, 1987; Poulton and Canfield, 2005
5	65% HNO_3	2	Mn HNO_3 Fe HNO_3	Mn bound to pyrite Pyrite	Lord III, 1982; Claff et al., 2010

3. Results

3.1. Sediment characteristics

Core PV1, from the Brillantes mudflat, consisted primarily of silty clays with alternating layers of very fine to fine sand showing evidence of bioturbation, that can be centimetric at 40, 55, 75, 95 cm depth for the first meter of the core, and decimetric at 120 cm depth (Fig.3A). The lower part of the core (from 360 cm depth to the bottom) consisted mainly of silty sands with sandy layers of few centimetres (470 and 550 cm depth) without any trace of bioturbation. The cores from the riverbed station present well-consolidated silty clayey mud in the top 30 cm depth (Fig.3, RR1-4b.i and RRK- 4b). Below, punctual layers of coarse sand mixed with clay are observed in RRK-4 whose widths vary from 1 cm to 10 cm (Fig.3C). The lower part of the core had a clayey-sandy aspect, characterised by the presence of well-consolidated silt level with the presence of some layers of fine sand and soft clay pebbles throughout the core at 117 cm depth.

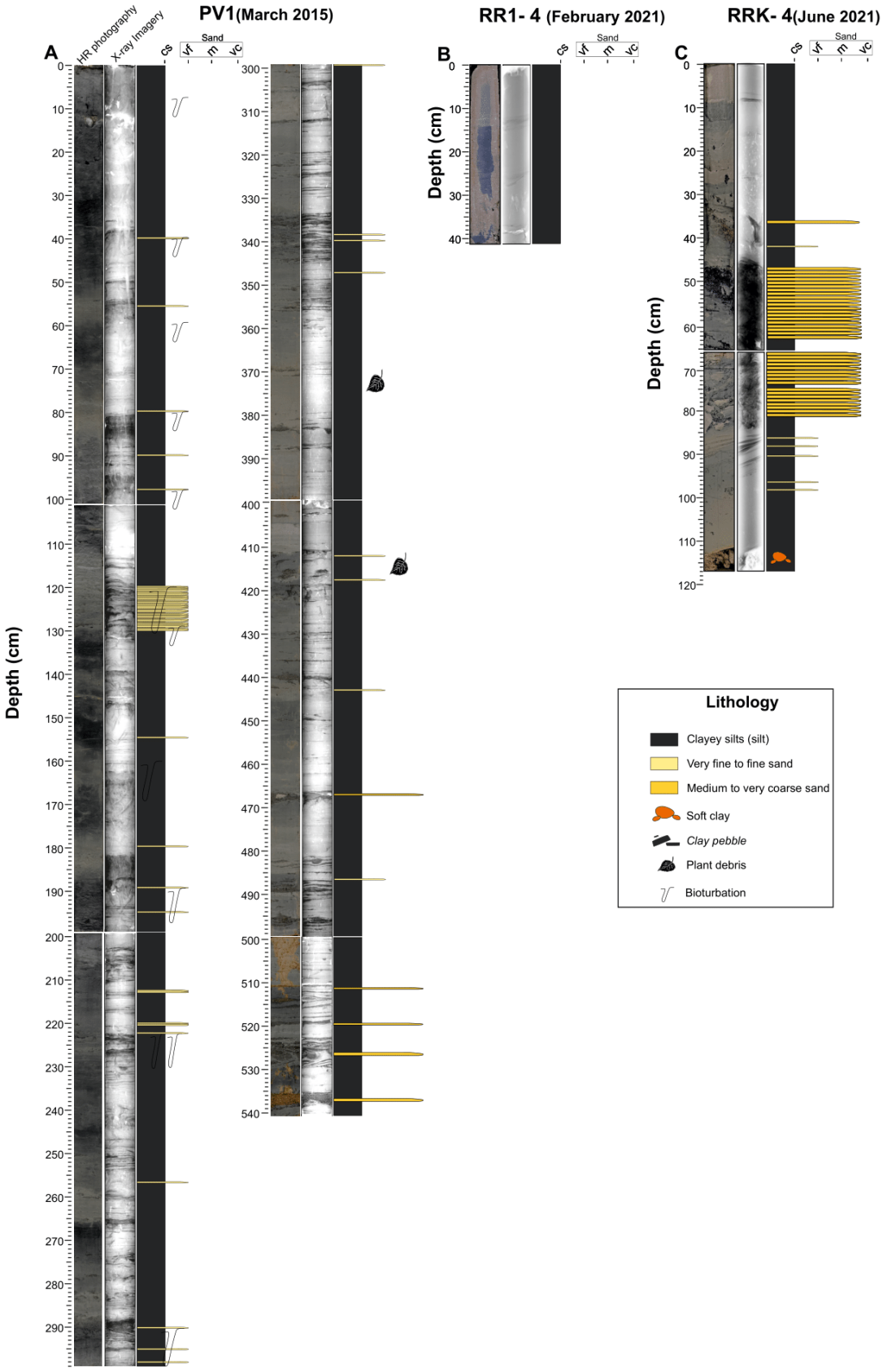

Fig 3. HD photographs, X-ray images and synthetic sedimentary columns of the 3 cores (PV1a, RR1-4a and RRK-4a) with their lithology. The light-coloured layers appearance observed on the X-ray images correspond to fine sediments, while the dark-coloured layers correspond to coarse sediments.

3.2. ^{210}Pb and ^{7}Be activities

For the Brillantes mudflat, $^{210}Pb_{xs}$ profile showed a surface mixed layer of 3-4 cm, with activity ranging around 90-100 mBq g^{-1}, followed by an exponential decrease with depth. Negligible excesses were reached deeper than 50 cm (Fig.4a).

For the muddy riverbed, the $^{210}Pb_{xs}$ profiles were quite different. While surface activities were also about 100 mBq g^{-1}, there was no significant decrease with depth in the upper 40 cm. In June 2021, there was still an excess of ^{210}Pb at the bottom of the long core (18±4 mBq g^{-1} at 172 cm; Fig.4c). On the other hand, ^{7}Be showed an important seasonal variability. In February 2021, during the flood event, ^{7}Be presented already negligible values in the upper sediment (0-1 cm) (Fig.4b). In June, ^{7}Be presented the highest activities in surface sediment (40 mBq g^{-1}), followed by a gradual decrease to reach 18 mBq g^{-1} at 34.5 centimetres (Fig.4c). In August, the surface ^{7}Be activities were also high (35 mBq g^{-1}) but decreased more rapidly with depth (Fig.4d).

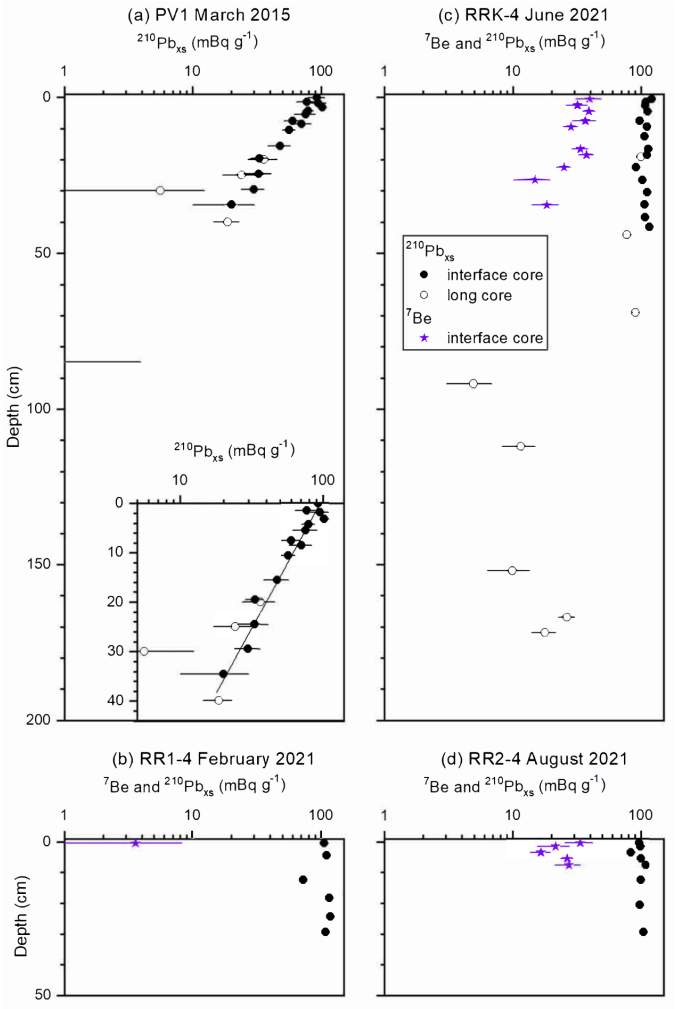

Fig 4. $^{210}Pb_{xs}$ and ^{7}Be profiles with depth in sediments of PV1 at the intertidal mudflat (a) and at the muddy riverbed during the cruises RR1 (b), RRK (c) and RR2 (d). Only interface cores were collected during RR1 and RR2 cruises. The inset in the figure 4a shows the exponential curve that was used to estimate the sedimentation rate of core PV1.

3.3. Porosity and pore-water profiles

Porosity on PV1 was 0.93 at the top core, gradually decreased to 0.78 at 25 cm depth (Fig.5A), increasing again to 0.82 at 50 cm depth, decreasing slightly with depth over 4 m, and decreasing rapidly from 5 m depth below 0.4. Off Paimboeuf, in February 2021 (RR1-4, Fig.5B), porosity at the top of the core was about 0.88 and remained constant throughout the profile. The long core collected in June at the same station (RRK-4) showed below 50 cm depth a decrease to 0.50 at 100 cm depth (Fig.5C). Porosity in August (RR2-4, Fig.5D) was around 0.98 at the surface, decreased to 0.90 in the first 5 cm, and then remained stable in the next 40 cm.

Vertical pore-water profiles of dissolved Mn (Mn_d), dissolved Fe (Fe_d), and sulphate showed significant variations throughout the cores from the intertidal mudflat (Fig.5A). Dissolved manganese presented a first intense and narrow maximum at 1 cm depth ($[Mn]_{max}$ = 262 µmol L^{-1} with FWHM = 5 cm) and a second light and smooth maximum between 40 to 125 cm depth ($[Mn]_{max}$ = 62 µmol L^{-1}) superimposed to a background concentration of about 20 µmol L^{-1}. Sulphate decreased from 10 mmol L^{-1} at the top of the core to depletion at 40 cm depth, which was defined as the sulphate penetration depth (SPD). Dissolved iron was almost absent in the first 3 cm before increasing to reach 78 µmol L^{-1} at 8 cm depth. Below this depth, Fe_d decreased to depletion at 25 cm depth. Below the SPD, Fe_d increased again and reached a maximum at 85 cm depth (461 µmol L^{-1}), followed by a decrease with depth along the rest of the core. It should be noted that the absence of data at the bottom of the cores was generally related to the absence or negligible amounts of pore-water in the samples, especially in sandy or coarse-grained layers. In the riverbed mudpatch, during winter (RR1-4), Mn_d and Fe_d presented much higher concentrations with more intense maximum ($[Mn]_{max}$ = 660 µmol L^{-1} at 5 cm depth, $[Fe]_{max}$ = 910 µmol L^{-1} at 20 cm depth) followed by a less pronounced decrease below ($[Mn]_{min}$ = 500 µmol L^{-1}, $[Fe]_{min}$ = 400 µmol L^{-1}). Sulphate concentrations at the surface sediment were about 6 µmol L^{-1} and increased to 12 mmol L^{-1} at 9 cm depth and then decreased to disappear at 50 cm depth. In June (RRK-4), Mn_d, Fe_d and sulphate profiles exhibited a specific pattern characterised by two peaks above the SPD at 8 cm depth and 44 cm depth. Maximum concentrations were higher in the deeper peak for redox metals while they presented similar concentrations of sulphate: $[Mn]_{max}$ = 460 and 530 µmol L^{-1}, $[Fe]_{max}$ = 270 µmol $L^{-1}$and 580 µmol L^{-1}, $[S]_{max}$ = 10 and 9.6 mmol $L^{-1}$for shallower and deeper peaks respectively. In August (RR2-4), dissolved element profiles showed the absence of Mn_d and Fe_d in the upper part of the core down to 2 cm depth (Fig.5D), followed by an increase to concentrations of 506 µmol L^{-1} for Mn_d and 313 µmol L^{-1} for Fe_d at 6.5 and 7.5 cm depth

respectively. Below this depth, Mn_d decreased to a concentration of 374 µmol L^{-1} at 19 cm depth and then increased to a maximum concentration of 586 µmol L^{-1} at 42.5 cm depth. Fe_d decreased sharply at 19 cm depth to attain a concentration of 46 µmol L^{-1} before reaching the maximum of 554 µmol L^{-1} at 42.5 cm depth. The SPD was not reached. Sulphate concentration decreased in the first 19 cm depth from 6.4 mmol L^{-1} to reach a minimum concentration of 0.16 mmol L^{-1} before increasing back to 5.8 mmol L^{-1} at 42.5 cm depth.

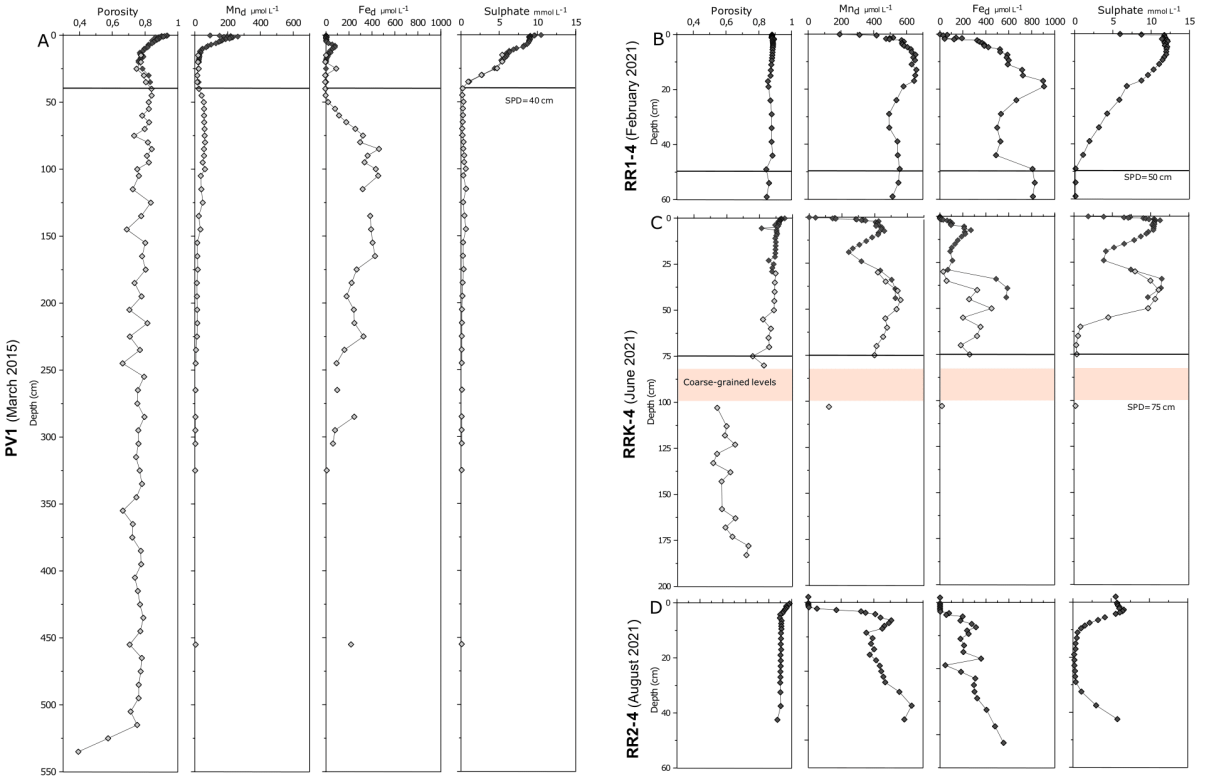

Fig 5. Porosity and pore-water profiles of dissolved Mn (Mn_d), dissolved Fe (Fe_d), and dissolved S (sulphate) concentrations with depth in PV1, RR1-4, RRK-4 and RR2-4. Horizontal black lines indicate the sulphate penetration depth (SPD), dark symbols representing interface cores (PV1b.i, RR1-4b.i, RRK-4b.i and RR2-4b.i) and clear symbols representing long cores (PV1b, RR1-4b, RRK-4b and RR2-4b) . The depth scale is different for each graphic.

3.4. Mn and Fe sequential extraction from the solid phase

Figure 6 illustrates the distribution of Mn and Fe phases for PV1, RR1-4 and RRK-4 according to the sequential extraction procedure. In the Brillantes mudflat (PV1; Fig.6A), most of the Mn and Fe phases showed a surface enrichment, except for oxalate-extracted Mn and HNO_3-extracted Mn and Fe. The highest concentration was observed for CDB-extracted Fe with 212 µmol g^{-1} at 3 cm depth. Ascorbate- and HCl-extracted Mn and Fe concentrations were 16.6 µmol $g^{-1}$and 77 µmol g^{-1}, 8.7 µmol g^{-1} and 196 µmol g^{-1}, respectively at the top of the core. CDB-extracted Mn also showed surface enrichment, albeit at lower concentrations (1.1 µmol g^{-1}). The extractible Mn enrichment zone was limited to the first 8 cm, while the extractible Fe enrichment zone extends to a depth of 20 cm. It should be noted that near the

surface, Fe was extracted in higher concentrations by HCl and CDB, and Mn by ascorbate and HCl. The HNO_3-extracted Mn and Fe presented a specific pattern with a peak between 20 and 30 cm depth at concentrations reaching 3.5 µmol g^{-1} and 193 µmol g^{-1} respectively. Below this depth, HNO_3-extracted Mn and Fe decreased sharply to a depth of 45 cm, reaching relatively stable concentrations of 0.4 µmol g^{-1} and 40 µmol g^{-1}, respectively, down to the core while HCl-extracted Fe and Mn exhibited an increase with increasing depth. At the muddy riverbed, RR1-4 showed low variations of all Mn and Fe phases with depth showing similar trends for Mn and Fe (Fig.6B). CDB-extracted Fe presented higher concentrations at around 180 µmol g^{-1} compared to ascorbate- and HCl-extracted Fe with around 60 µmol g^{-1} and 170 µmol g^{-1} respectively, while for Mn, the highest concentrations were observed for HCl-extracted Mn with around 18 µmol g^{-1} compared to ascorbate- and CDB-extracted Mn with 11 µmol g^{-1} and 1.5 µmol g^{-1} respectively. For the other phases, concentrations remained consistently low throughout the core. HNO_3-extracted Mn and Fe were around 0.35 µmol g^{-1} and 34 µmol g^{-1} respectively, and for oxalate-extracted Mn and Fe, concentrations were around 0.37 µmol g^{-1} and 41 µmol g^{-1} respectively. In June, at the same station, RRK-4 showed a clear gradient between levels, above and below the coarser-grained layers (Fig.6C). Above the coarser-grained layers, concentrations of Mn and Fe phases showed relatively consistent variations with depth. In particular, HNO_3-extracted Mn and Fe remained stable regardless of depth, while concentrations of other phases increased at 80 cm depth. Below the coarser-grained layers, ascorbate-HCl- CDB- and oxalate-extracted Mn and Fe showed an increasing trend with depth, reaching their highest concentrations at 183 cm depth. For HNO_3-extracted Mn and Fe, the highest concentrations were reached at a depth of 125 cm.

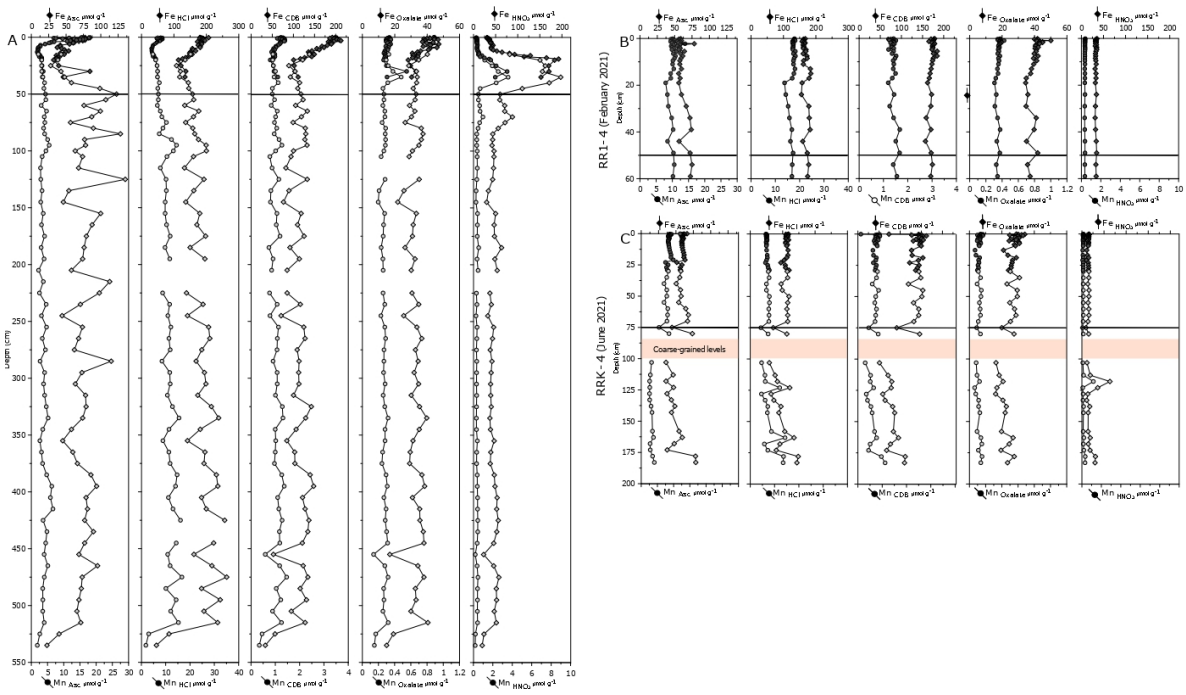

Fig 6. Solid phase depth profiles of different forms of Mn and Fe in PV1, RR1-4 and RRK-4 as determined with the sequential extraction procedure showing poorly ordered Mn oxides and ferrihydrite (Mn Asc and Fe Asc), Mn and Fe carbonates, reducible crystalline Fe oxides, mackinawite and vivianite (Mn HCl and Fe HCl), Mn and Fe crystalline oxides (Mn CDB and Fe CDB), Mn recalcitrant oxides and magnetite (Mn oxalate and Fe oxalate), and Mn bound to pyrite (Mn HNO_3 and Fe HNO_3). Circles represent Mn and squares represent Fe. Dark symbols represent interface cores (PV1b.i, RR1-4b.i, RRK-4b.i and RR2-4b.i), while clear symbols represent long cores (PV1b, RR1-4b, RRK-4b and RR2-4b). Depth scale is different for each graphic.

4. Discussion

4.1. Temporal context and sedimentary dynamics

Sediment dynamics in estuaries play a critical role in shaping these coastal ecosystems. A number of processes take place in these environments, including remobilization of previously deposited sediments and temporary interruptions in deposition (e.g. Deflandre et al., 2002). PV1 core is composed mainly of silty clays, indicating a relatively calm environment. The application of the CF:CS model to PV1 $^{210}Pb_{xs}$ profile had permitted to estimate a mean sedimentation rate of 0.7 cm yr^{-1} for the top 40 centimetres of the record.

At the riverbed, in February 2021 (RR1-4), the high cohesivity, the dark colour and the relatively low and constant porosity of the interface core sediment suggest a stable and well-consolidated composition primarily consisting of silty clayey mud (Fig.3B, 5B). The negligible ^{7}Be in surface sediments tends to indicate the absence of recent sediment deposition (Fig.4B). In June (RRK-4), we observed various sediment types and structures at different depths (Fig.3C) indicating variable depositional conditions. In particular, the presence of a distinct coarse to very coarse sand layer in the middle of the core (from 45 to 85 cm depth) strongly suggests that the environment experienced a period of higher energy and

more dynamic conditions, probably related to an unusually high river discharge or a marine storm (Edmiston et al., 2008).

After the February exceptional flood (Fig.2), the water discharge decreased from 4300 to 384 m^3 s^{-1} in June, which led to favourable conditions for a shift of the TMZ upstream. Accordingly, the rather constant activities of $^{210}Pb_{xs}$ in the top 70 cm support a single and recent (< 5 years) deposition event (Fig.4c). The ^{7}Be signal allows more precise investigation with the top 20 cm being less than 1 month old while the sediments at 34 cm are estimated to be about 62 days by applying the CIC model to ^{7}Be. These elements offer valuable insights into the timing and dynamics of recent deposition events in the muddy riverbed, which experiences episodes of resuspension/sedimentation of variable intensity depending on fluvial discharge and the position of the TMZ. This hydrodynamical context prevents the regular accumulation of fine sediment in the estuarine bed, unlike the nearby intertidal mudflat, and creates non-steady state conditions.

4.2. Mn and Fe cycling in the Brillantes mudflat

In the upper 10 cm of PV1, Mn_d and Fe_d are successively released towards pore-water (Fig.5A). The increase in Mn_d with ascorbate-extracted Mn decrease in the first centimetre can be attributed to reductive dissolution of reactive Mn oxides. The same process can be seen for Fe a few centimetres below, as Fe_d gradually increases from 3 cm depth, indicating a transition of the dominant oxidant from Mn oxides to Fe oxides (ascorbate-extracted Fe). According to Thibault de Chanvalon et al. (2016), the well-established and separated peaks of Mn and Fe suggest that the transitional phase of diagenetic processes after flood deposition is already in a fairly stable condition. Furthermore, the surface concentration of ascorbate-extracted metals corresponded to Loire suspended particles composition (Thibault de Chanvalon et al., 2016b) indicating negligible metal diagenetic enrichment contrasting with frequent observation in continental margins systems (Anschutz et al., 1998; Mouret et al., 2009). Once reductively dissolved, Fe and Mn can either leave the sediment or reprecipitate generally as carbonates, sulphides or phosphates (Aller, 2014).

Sulphate concentrations in PV1 showed a complete depletion at 40 cm depth (Fig.5A), suggesting that sulphate is consumed as the dominant oxidant between 10 cm and 40 cm depth for metabolic processes and/or as an anaerobic oxidant of methane (not measured in this study but likely produced by methanogenesis after the total depletion of sulphate (Burdige, 2006)). This layer corresponds to a depletion of Fe_d (Fig.5A) and the maximum of HNO_3-extracted Fe and associated Mn (Fig.6A), suggesting that Fe sulfides formation is important at

this depth. The formation of iron sulphides in sediments is a complex process influenced by several factors, such as the amount and reactivity of organic matter, reactive iron minerals deposited in the sediment, and the availability of dissolved sulphate (Berner, 1984). The residence time of particles in sediments can also affect FeS/FeS_2 formation. Pyrite formation may occur where the deposition rate is very high (Berner, 1984) as it is observed in the Brillantes mudflat.

Below 40 cm depth, the HNO_3-extracted Mn and Fe decrease (Fig.6A) would indicate that iron sulphides production stops limiting their burial in the sediment archives. The lack of FeS/FeS_2 formation is well explained by the absence of sulphate at that depth which prevents sulphide formation (Fig.5A). However, it is difficult to explain the absence of FeS/FeS_2 burial while this mineral is commonly observed in geological records and is known to be stable in anoxic conditions (Berner, 1980; Rickard and Luther, 2007). The distinct enrichment in Fe_{HNO3} between 10 and 40 cm depth could therefore indicate non-steady state conditions due to increased inputs of organic matter induced by human activities, as previously observed in other environments with similar FeS/FeS_2 records (e.g. Egger et al., 2015; Slomp et al., 2013). Between 40 and 50 cm depth, the decrease of Fe_{HNO3} occurs simultaneously to an increase of Fe_{ASC} (Fig.6A). Ferrihydrite formation is unlikely due to the lack of oxidant at these depths but other minerals such as vivianite or illite-bound metals (W. K. Lenstra et al., 2021; Rennert et al., 2021) can be extracted with the ascorbate reagent. Several studies showed the possible formation of vivianite below the sulphate/methane transition zone (e.g. Egger et al., 2015; Kubeneck et al., 2021; Rothe et al., 2015). Deeper, between 50 cm to 300 cm depth, a progressive increase in HCl-extractable Mn and Fe coincide with the highest Fe_d measured in this core and an increase in Mn_d, reinforcing the impression of a slow formation of Mn and Fe carbonates as end member of the early diagenesis transformation. The high dissolved metal concentrations in the pore- water could be explained by several processes (Slomp et al., 2013). A first mechanism is the reduction of Fe and Mn oxides coupled to organic matter degradation. Although these pathways are energetically more favourable than sulphate reduction, studies that focused on Fe suggested that kinetic control may limit the rate and extent of Fe oxide reduction (Postma, 1967; Sivan et al., 2011). This kinetic limitation would favour the persistence of unsulphidized Fe oxides (März et al., 2008; Xiong et al., 2019) allowing their reduction below the SPD. Another possible mechanism is the oxidation of methane with Mn and Fe oxides (Beal et al., 2009; Cai et al., 2018; Leu et al., 2020). Finally, Ma et al., (2023) demonstrated recently that the dissolution of mackinawite (FeS) releases HS^-, which can be removed by transport or oxidation, and Fe_d, which can react with phosphate to

precipitate vivianite. The increase of Fe_d below 50 cm depth occurs simultaneously with an almost equimolar increase of sulphate (Fig.5A), which could be induced by the dissolution of this metastable intermediate in the pyrite formation process. There is no extractive step presenting a symmetric decrease to the presence of dissolved iron and manganese accumulation in the pore-water below 50 cm depth. Contrastingly, CDB- and oxalate-extractable Mn and Fe represent a constant fraction, indicating the burial of less reactive/non-reactive forms in the sediment (Lenstra et al., 2019; W. K. Lenstra et al., 2021).

The observed diagenetic sequence of Mn and Fe in the Brillantes mudflat can be summarized as the following sequence: (1) deposition of reactive riverine Fe and Mn oxides, then (2) reduction of metal oxides by bacterial respiration or by sulphide from depth, (3) precipitation of sulphide mineral such as mackinawite or pyrite, then (4) transition from FeS/FeS_2 formation to vivianite formation and pore-water enrichment, finally (5) precipitation at depth of Mn and Fe carbonate depleting Mn_d and Fe_d from the pore-water. This sequence highlights the complex interplay between sedimentary processes evolving geochemical conditions in the different layers of the Brillantes mudflat. Up to stage 3, the present study is in agreement with the processes highlighted in the upper St-Lawrence estuary (Lefort et al., 2012; Oldham et al., 2019). However, both studies are based on 20 and 50 cm-deep cores and missed ultimate burial processes that highlight the importance of phosphates and carbonates to authigenic formation (stages 4 and 5). Another difference is the significative burial of Mn as carbonates in the Loire. Oldham et al., (2019) attributed the limited Mn burial to the important amount of Mn(III)-organic ligands complexes in pore-water favouring mobility during early diagenesis. In the Vörå creek estuary, located in the Finnish Baltic Sea, the study of Fe solid speciation from a long core (4.5m) showed another feature. Fe oxides were fairly stable along the sedimentary series (stage 1; Yu et al., 2015). The authors attributed this feature to the lack of sulphate that limits the formation of sulphur compounds despite a high sedimentary rate and an important organic carbon content. This is probably representative of the Bothnian Gulf estuaries as Widerlund and Ingri, (1996) showed the same efficiency of Mn and Fe oxides burial in the Kalix estuary.

4.3. Early diagenesis in the estuarine bed subjected to hydrodynamic events

In February 2021, the remarkable flood of the Loire resulted in significant erosion of surface sediments in the upper estuary, including the muddy riverbed at Paimboeuf, revealing to the water column a very dark and cohesive sediment with some gas ebullition (Hulot et al., 2023). The geochemical signature of the surface sediments sampled after the erosion (RR1-4)

was characterised by relatively high and constant concentrations of different extracted Mn and Fe phases compared to PV1 (Fig.6B). Sharp pore-water gradients for Mn_d, Fe_d and sulphate at the SWI indicated the sudden exposure of the old ^{7}Be-free and anoxic sediment (Fig.4b) to low salinity, well oxygenated waters. In the surface sediment, Mn_d and Fe_d were high with no enrichment of ascorbate-extracted Mn and Fe. The same geochemical signatures were documented 24 km upstream (RR1-2) during the same sampling cruise (Hulot et al., 2023). This erosion phenomenon at the muddy riverbed had a significant impact on iron sulphides formation in the sediment. Despite sulphate reduction (attested by the decrease of S/Na in pore-water, see Supplementary Fig.S1), no Mn and Fe peaks were observed in the HNO_3 extracted fraction in this core (Fig.6B). This is probably related to the adjustment of the sulphate-methane transition zone following the intense erosional forces triggered by this extraordinary flood event. This erosion process disturbed the otherwise stable sedimentary layers, interrupted chemical reactions that occur in a steady-state context, and shifted redox conditions (changes in the availability of oxygen and other electron acceptors) within the sediment which explains the relatively constant concentrations of Mn and Fe particulate/mineral phases, especially HNO_3-extracted Mn and Fe.

In June 2021, about four months later, the decreased low river discharge recorded during the sampling cruise (about 384 m^3 s^{-1}) resulted in favourable conditions for an upstream shift of the TMZ above the studied area of the river (Fig.1; Fig.2). The rather constant $^{210}Pb_{xs}$ activities in the interface core (RRK-4b.i) and the ^{7}Be penetration up to 30 cm indicated either active bioturbation or recent and high sediment deposition (Fig.4c), the latter being more likely according to X-ray images from the topmost layer of the Kullenberg core (RRK-4a) that showed a very fine and homogenous deposit (Fig.3), and to the double peak observed in pore-water profiles. This phenomenon is consistent with documented cases of deposition of TMZ-derived particles in macrotidal estuaries (Grabemann et al., 1997; Migniot, 1972; Woodruff et al., 2001). Based on these observations (Fig.4 and 7), it is likely that this sediment deposition occurred between March and June 2021 and its thickness can be estimated at around 30 cm. This deposit was characterised by Mn_d and Fe_d peaks associated with a zone of intense, localized production, separated from another production zone observed at 30 cm depth (Fig.7). It is likely that these deeper peaks of Mn_d and Fe_d are the legacy of the remobilization layer below the previous SWI and corresponded to the production observed in February 2021 (Fig.7). Mn and Fe oxides (ascorbate-extracted Mn and Fe) remained high and constant at the new SWI and below (Fig.6C). Several studies have already highlighted the significant effects of turbidity deposition on benthic communities and diagenetic processes in

525 the sediment (Mucci and Edenborn, 1992). Typically, after the deposition event, oxygen
526 quickly re-establishes in the uppermost part of the freshly deposited layer, allowing Mn and
527 Fe oxides to accumulate by oxidation of Mn_d and then Fe_d diffusing from the underlying
528 layers (Anschutz et al., 2002; Deflandre et al., 2002; Guilhermic, 2023). The absence of
529 significant variation of Mn and Fe oxides within the first centimetres of RRK-4 sediment
530 (Fig.6C) suggests that the fresh deposit rich in metal oxides started to be consumed recently.
531 In the same core (RRK-4), below the coarse layers, there is a marked decrease in the
532 occurrence of Mn and Fe phases. A low peak in HNO_3-extracted Mn and Fe at 125 cm depth
533 could correspond to the formation of iron sulphides. The fact that FeS/FeS_2 can be present at
534 this depth indicates that the specific conditions for FeS/FeS_2 formation were met at some time
535 in the history of the sediment suggesting calmer hydrodynamic conditions over a period that
536 can hardly be dated.
537 In August (RR2-4), about 6 months after the flood, Mn_d, Fe_d and sulphate double peaks
538 observed in June were much less marked for Mn and especially for Fe while sulphate showed
539 a downward shift of its second peak, the first remaining at the SWI despite a concentration
540 decrease. These observations strongly indicate that both Mn_d and Fe_d that were located more
541 than 30 centimetres below the surface (i.e., the RRK-4 second peak) were likely able to
542 undergo precipitation, potentially forming carbonates or sulphides as shown in the muddy
543 sediments of the Bay of Biscay (Hyacinthe et al., 2001). In the new SWI, the decrease of Mn_d
544 and Fe_d within the first 2 and 3 centimetres respectively (Fig.5D) strongly suggests their
545 precipitation into Mn and Fe oxides that would generate an enriched metal-oxide layer as
546 observed from ascorbate extracted Mn and Fe. The attenuation of Mn_d, Fe_d and sulphate
547 double peaks observed between June and August is indicative of redox fronts undergoing
548 relaxation within this recently deposited layer (Guilhermic, 2023). The time required for the
549 recovery process, known as the relaxation time, is influenced by several factors, including
550 sediment porosity, the grain size, organic matter content and thickness of the deposit (Nmor
551 et al., 2022). It is important to note that different species have different recovery rates in pore-
552 water. For example, oxygen can recover within a few days (Cathalot et al., 2010) while
553 sulphate takes around four months to recover (Nmor et al., 2022). In addition, Chaillou et al.
554 (2007) indicate that it can take about several months for both Mn and Fe to fully recover after
555 turbidite deposition or even years in Canadian fjords (Deflandre et al., 2002). Our results of
556 August show that the recovery of Mn_d, Fe_d and sulphate steady-state levels is not yet
557 complete. These transient conditions illustrate the dynamic nature of estuarine environments,
558 where complex interactions between physical, chemical and biological factors constantly

shape the geochemical profiles of Mn and Fe and influence their availability, speciation and cycling within the sediment matrix, resulting in a lack of thermodynamic equilibrium between the dissolved and solid phases with, for example, the absence of FeS/FeS_2 accumulation within the sediment in the estuarine bed.

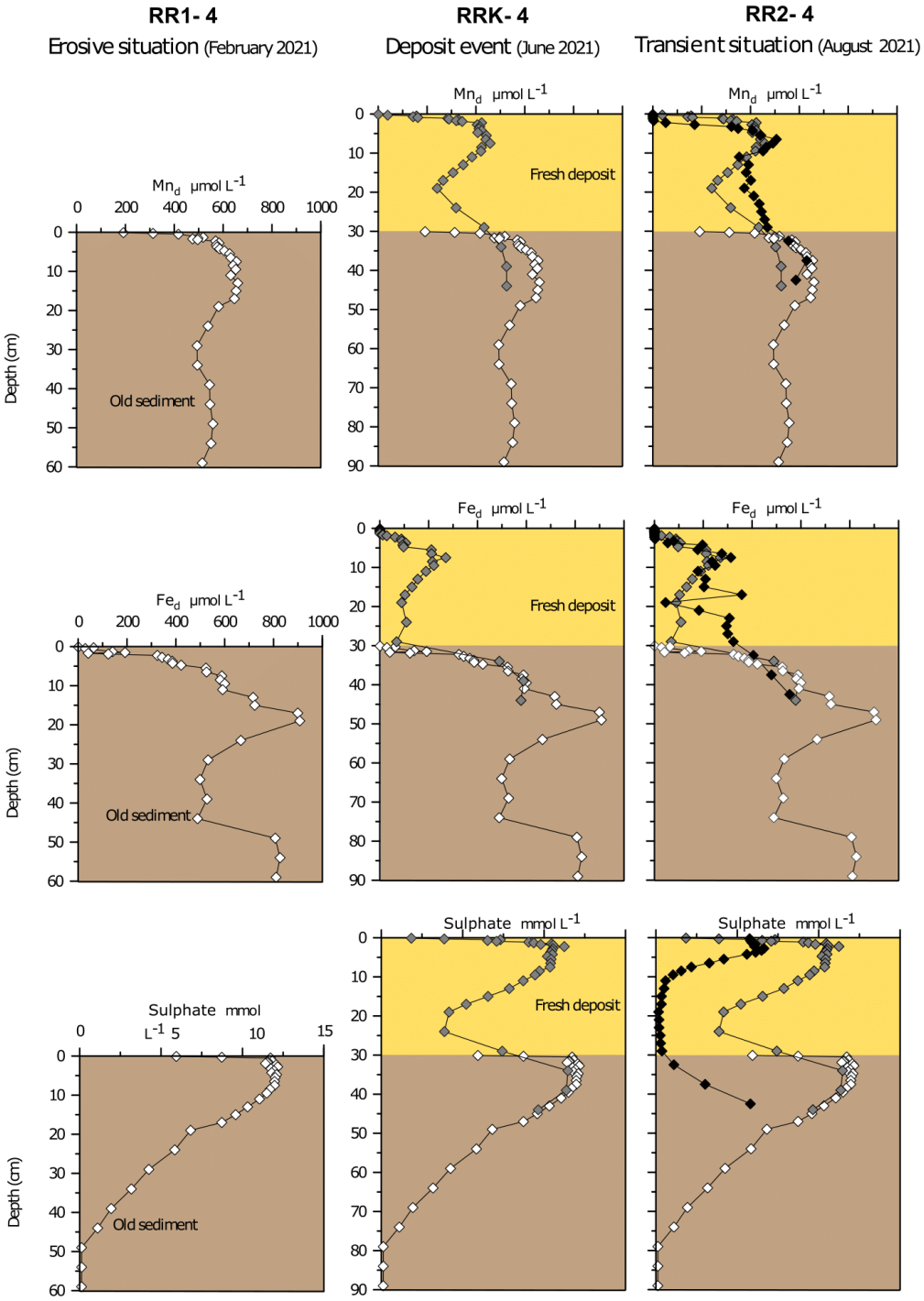

Fig 7. Pore-water profiles of dissolved Mn (Mn_d), dissolved Fe (Fe_d), and sulphate concentrations with depth, temporally contextualized after a hydrosedimentary interpretation based on radioelements at the muddy riverbed (Paimboeuf) in winter, spring, and summer 2021. White squares show February data, dark grey squares show June data, and black squares show August data.

5. Conclusion

The present study sheds light on the dynamic interplay of Mn and Fe in early diagenetic processes of burial and recycling in the Loire mid-estuary, in two different hydrodynamic contexts regarding deposition/resuspension, a muddy riverbed near the navigation channel and the major intertidal mudflat nearby. The 5m-long cores sampled at the Brillantes intertidal mudflat showed a sequence of authigenic mineral formation with a transition within the first metre from an expected FeS/FeS_2 formation layer and a layer of another authigenic phase which could be vivianite, probably because of a past higher organic matter production in the estuary under the influence of human activities. Finally, the slow formation of Mn and Fe carbonates constitutes an end member of the early diagenesis transformation. This intricate interplay between dissolution, precipitation and redox transformations underlines the complex relationship between sedimentary processes and the several pathways for the recycling and ultimate burial of Mn and Fe at different depths of the Brillantes mudflat that alters the sedimentary archive.

Within the river, the February flood event had a significant impact on the sediment, causing erosion and subsequent changes in the geochemical signature. The intense erosional forces ruptured stable sediment layers and prevented effective conversion of dissolved constituents to solid phases. This resulted in low and constant concentrations of Mn and Fe solid phases, especially ascorbate and HNO_3-extracted Mn and Fe (amorphous oxides and pyrite or pyrite-bound Mn, respectively). The subsequent lowering of the river discharge allowed the formation of a 30 cm-thick deposit layer four months later, in June. The new deposit generated a second metal remobilisation zone 30 cm above the previous one still visible despite the distance from the new SWI. Progressively this peculiar feature evolved towards a more classic redox zonation. The high sedimentary dynamics in this riverbed generated transient conditions illustrating the dynamic nature of estuarine environments, where complex interactions between physical, chemical and biological factors influence the availability, speciation and cycling of Mn and Fe within the sediment matrix. This transient state leads to a lack of thermodynamic equilibrium between dissolved and solid phases with, for example, no FeS/FeS_2 accumulation within the sediment of the estuarine bed.

The well-established burial diagenetic sequence observed in the Loire estuarine mudflats differs from the observation made in the St-Lawrence and estuaries form the Bothnian Gulf. The St-Lawrence is characterized by little burial of Mn and important burial of Fe sulphides while the Bothnian Gulf estuaries show little transformation of trapped particles with efficient burial of reactive oxides. The Loire estuary mudflats show that these metals are buried as

carbonates and phosphates following a more complex sequential transformation and could represent another burial pathway typical for temperate macrotidal estuaries which catchment provides detrital reactive oxides and carbonates.

Investigating the behaviour of Mn and Fe in sediments holds considerable potential for improving the quality of estuarine systems. Our research in this area provide valuable insights into disruption of sedimentation patterns and subsequent rebalancing in these dynamic environments. These studies are particularly important for estuarine systems, which are characterised by complicated interactions between solid and dissolved phases. Understanding the non-equilibrium dynamics of these systems is critical as they deviate from traditional steady-state conditions and require a nuanced understanding especially when interpreting sedimentary historical records. Recognizing that sediment is both a source and a sink for essential nutrients such as Mn and Fe and their recycling by-products is critical for developing comprehensive strategies to improve the overall water quality of estuarine ecosystems.

Acknowledgments

This research was supported by the scientific projects REBELRED funded by CNRS (National Center for Scientific Research) and OFB (French Biodiversity Office), DEPEL funded by GPMNSN (the Grand maritime port of Nantes Saint-Nazaire), PALEOVASE funded by OSUNA (Observatory of Earth Sciences of Nantes - CNRS-INSU / IN2P3), and the integrated project (IP) LIFE REVERS'EAU (LIFE19 IPE/FR/000007). Radionuclides measurement of core PV1 was self-funded by EPOC. REBELRED cruises were supported by the TGIR Flotte Océanique Française (doi.org/10.17600/18001620). Authors heartly thank Didier Lehay from the GPMNSN for his support, and Bernadette Tessier, Sylvain Haquin and Franck Lelong, from the M2C laboratory in Caen (UMR CNRS 6143) for providing us with the necessary equipment and technical help to sample core PV1. Authors want to thank the crews of RV Thalia and RV Côtes de la Manche for their valuable work sampling under extreme conditions. The multicorer used during the Rebelred cruises was provided by EPOC. The Paleovase cores were sampled with a percussion corer from M2C Caen on board the La Brise. Special thanks to Vivien Hulot, Yohann Poprawski, Lisa Nauton, Amanda Perrin, Eloi Marilleau, Hélène Howa, Nicolas Dubosq, Anthony Barbe, Livia Defaye, Romain Levrard for their help and support during sampling and laboratory analyses.

References

Allen, G.P., Salomon, J.C., Bassoullet, P., Du Penhoat, Y., de Grandpré, C., 1980. Effects of tides on mixing and suspended sediment transport in macrotidal estuaries. Sedimentary Geology 26, 69–90. https://doi.org/10.1016/0037-0738(80)90006-8

Aller, R.C., 2014. Sedimentary diagenesis, depositional environments, and benthic fluxes.

Aller, R.C., Charnock, H., Edmond, J.M., McCave, I.N., Rice, A.L., Wilson, T.R.S., 1997. Bioturbation and manganese cycling in hemipelagic sediments. Philosophical Transactions of the Royal Society of London. Series A, Mathematical and Physical Sciences 331, 51–68. https://doi.org/10.1098/rsta.1990.0056

Anschutz, P., Dedieu, K., Desmazes, F., Chaillou, G., 2005. Speciation, oxidation state, and reactivity of particulate manganese in marine sediments. Chemical Geology 218, 265–279. https://doi.org/10.1016/j.chemgeo.2005.01.008

Anschutz, P., Jorissen, F.J., Chaillou, G., Abu-Zied, R., Fontanier, C., 2002. Recent turbidite deposition in the eastern Atlantic: Early diagenesis and biotic recovery. Journal of Marine Research 60, 835–854. https://doi.org/10.1357/002224002321505156

Anschutz, P., Zhong, S., Sundby, B., Mucci, A., Gobeil, C., 1998. Burial efficiency of phosphorus and the geochemistry of iron in continental margin sediments. Limnology and Oceanography 43, 53–64. https://doi.org/10.4319/lo.1998.43.1.0053

Beal, E.J., House, C.H., Orphan, V.J., 2009. Manganese- and Iron-Dependent Marine Methane Oxidation. Science 325, 184–187. https://doi.org/10.1126/science.1169984

Berner, R.A., 1984. Sedimentary pyrite formation: An update. Geochimica et Cosmochimica Acta 48, 605–615. https://doi.org/10.1016/0016-7037(84)90089-9

Berner, R.A., 1980. Early Diagenesis: A Theoretical Approach. Princeton University Press.

Burdige, D.J., 2006. Geochemistry of Marine Sediments, in: Geochemistry of Marine Sediments. Princeton University Press. https://doi.org/10.1515/9780691216096

Burdige, D.J., 1993. The biogeochemistry of manganese and iron reduction in marine sediments. Earth-Science Reviews 35, 249–284. https://doi.org/10.1016/0012-8252(93)90040-E

Cai, C., Leu, A.O., Xie, G.-J., Guo, J., Feng, Y., Zhao, J.-X., Tyson, G.W., Yuan, Z., Hu, S., 2018. A methanotrophic archaeon couples anaerobic oxidation of methane to Fe(III) reduction. The ISME Journal 12, 1929–1939. https://doi.org/10.1038/s41396-018-0109-x

Canfield, D.E., 1993. Organic Matter Oxidation in Marine Sediments, in: Wollast, R., Mackenzie, F.T., Chou, L. (Eds.), Interactions of C, N, P and S Biogeochemical Cycles and Global Change, NATO ASI Series. Springer, Berlin, Heidelberg, pp. 333–363. https://doi.org/10.1007/978-3-642-76064-8_14

669 Cathalot, C., Rabouille, C., Pastor, L., Deflandre, B., Viollier, E., Buscail, R., Grémare, A.,
670 Treignier, C., Pruski, A., 2010. Temporal variability of carbon recycling in coastal sediments
671 influenced by rivers: assessing the impact of flood inputs in the Rhône River prodelta.
672 Biogeosciences 7, 1187–1205. https://doi.org/10.5194/bg-7-1187-2010
673 Chaillou, G., Anschutz, P., Dubrulle, C., Lecroart, P., 2007. Transient States in Diagenesis
674 Following the Deposition of a Gravity Layer: Dynamics of O2, Mn, Fe and N-Species in
675 Experimental Units. Aquat Geochem 13, 157–172. https://doi.org/10.1007/s10498-007-9013-
676 0
677 Charles J. Lord, I.I.I., 1982. A Selective and Precise Method for Pyrite Determination in
678 Sedimentary Materials: RESEARCH-METHOD PAPER. Journal of Sedimentary Research
679 52.
680 Chester, R., Hughes, M.J., 1967. A chemical technique for the separation of ferro-
681 manganese minerals, carbonate minerals and adsorbed trace elements from pelagic sediments.
682 Chemical Geology 2, 249–262. https://doi.org/10.1016/0009-2541(67)90025-3
683 Ciffroy, P., Reyss, J.-L., Siclet, F., 2003. Determination of the residence time of suspended
684 particles in the turbidity maximum of the Loire estuary by 7Be analysis. Estuarine, Coastal
685 and Shelf Science 57, 553–568. https://doi.org/10.1016/S0272-7714(02)00339-6
686 Claff, S.R., Sullivan, L.A., Burton, E.D., Bush, R.T., 2010. A sequential extraction
687 procedure for acid sulfate soils: Partitioning of iron. Geoderma 155, 224–230.
688 https://doi.org/10.1016/j.geoderma.2009.12.002
689 DATA.SHOM, 2024. . Portail d'informations géographiques maritimes de référence. URL
690 https://data.shom.fr/ (accessed 3.20.24).
691 Deflandre, B., Mucci, A., Gagné, J.-P., Guignard, C., Sundby, B. jørn, 2002. Early
692 diagenetic processes in coastal marine sediments disturbed by a catastrophic sedimentation
693 event. Geochimica et Cosmochimica Acta 66, 2547–2558. https://doi.org/10.1016/S0016-
694 7037(02)00861-X
695 Edmiston, H.L., Fahrny, S.A., Lamb, M.S., Levi, L.K., Wanat, J.M., Avant, J.S., Wren, K.,
696 Selly, N.C., 2008. Tropical Storm and Hurricane Impacts on a Gulf Coast Estuary:
697 Apalachicola Bay, Florida. Journal of Coastal Research 38–49. https://doi.org/10.2112/SI55-
698 009.1
699 Egger, M., Jilbert, T., Behrends, T., Rivard, C., Slomp, C.P., 2015. Vivianite is a major
700 sink for phosphorus in methanogenic coastal surface sediments. Geochimica et
701 Cosmochimica Acta 169, 217–235. https://doi.org/10.1016/j.gca.2015.09.012

Froelich, P.N., Klinkhammer, G.P., Bender, M.L., Luedtke, N.A., Heath, G.R., Cullen, D., Dauphin, P., Hammond, D., Hartman, B., Maynard, V., 1979. Early oxidation of organic matter in pelagic sediments of the eastern equatorial Atlantic: suboxic diagenesis. Geochimica et Cosmochimica Acta 43, 1075–1090. https://doi.org/10.1016/0016-7037(79)90095-4

Gallene, B., 1974. Les accumulations turbides de l'estuaire de la Loire. Etude de la crème de vase. Nantes.

GIP Loire, 2023. La dynamique du bouchon vaseux, Cahiers indicateurs GIP Loire Estuaire, L1.E2, 8p.

Grabemann, I., Uncles, R.J., Krause, G., Stephens, J.A., 1997. Behaviour of Turbidity Maxima in the Tamar (U.K.) and Weser (F.R.G.) Estuaries. Estuarine, Coastal and Shelf Science 45, 235–246. https://doi.org/10.1006/ecss.1996.0178

Guilhermic, C., 2023. Effets des instabilités sédimentaires sur les microhabitats benthiques : cas du Kongsfjorden. Angers.

Hulot, V., Metzger, E., Thibault de Chanvalon, A., Mouret, A., Schmidt, S., Deflandre, B., Rigaud, S., Beneteau, E., Savoye, N., Souchu, P., Le Merrer, Y., Maillet, G.M., 2023. Impact of an exceptional winter flood on benthic oxygen and nutrient fluxes in a temperate macrotidal estuary: Potential consequences on summer deoxygenation. Frontiers in Marine Science 10.

Hyacinthe, C., Anschutz, P., Carbonel, P., Jouanneau, J.-M., Jorissen, F.J., 2001. Early diagenetic processes in the muddy sediments of the Bay of Biscay. Marine Geology 177, 111–128. https://doi.org/10.1016/S0025-3227(01)00127-X

Hydro B, 2021. . Banque nationale de donnée pour l'hydrométrie et l'hydrologie. banque hydro, ministère de l'Environement et du développement durable (Paris). URL https://www.hydro.eaufrance.fr/ (accessed 6.20.23).

Jalón-Rojas, I., Schmidt, S., Sottolichio, A., Bertier, C., 2016. Tracking the turbidity maximum zone in the Loire Estuary (France) based on a long-term, high-resolution and high-frequency monitoring network. Continental Shelf Research 117, 1–11. https://doi.org/10.1016/j.csr.2016.01.017

Kostka, J.E., Luther, G.W., 1994. Partitioning and speciation of solid phase iron in saltmarsh sediments. Geochimica et Cosmochimica Acta 58, 1701–1710. https://doi.org/10.1016/0016-7037(94)90531-2

Kubeneck, L.J., Lenstra, W.K., Malkin, S.Y., Conley, D.J., Slomp, C.P., 2021. Phosphorus burial in vivianite-type minerals in methane-rich coastal sediments. Marine Chemistry 231, 103948. https://doi.org/10.1016/j.marchem.2021.103948

Lefort, S., Mucci, A., Sundby, B., 2012. Sediment Response to 25 Years of Persistent Hypoxia. Aquat Geochem 18, 461–474. https://doi.org/10.1007/s10498-012-9173-4

Lenstra, W.K., Hermans, M., Séguret, M.J.M., Witbaard, R., Behrends, T., Dijkstra, N., van Helmond, N.A.G.M., Kraal, P., Laan, P., Rijkenberg, M.J.A., Severmann, S., Teacă, A., Slomp, C.P., 2019. The shelf-to-basin iron shuttle in the Black Sea revisited. Chemical Geology 511, 314–341. https://doi.org/10.1016/j.chemgeo.2018.10.024

Lenstra, Wytze K., Hermans, M., Séguret, M.J.M., Witbaard, R., Severmann, S., Behrends, T., Slomp, C.P., 2021. Coastal hypoxia and eutrophication as key controls on benthic release and water column dynamics of iron and manganese. Limnology and Oceanography 66, 807–826. https://doi.org/10.1002/lno.11644

Lenstra, W. K., Klomp, R., Molema, F., Behrends, T., Slomp, C.P., 2021. A sequential extraction procedure for particulate manganese and its application to coastal marine sediments. Chemical Geology 584, 120538. https://doi.org/10.1016/j.chemgeo.2021.120538

Leu, A.O., Cai, C., McIlroy, S.J., Southam, G., Orphan, V.J., Yuan, Z., Hu, S., Tyson, G.W., 2020. Anaerobic methane oxidation coupled to manganese reduction by members of the Methanoperedenaceae. The ISME Journal 14, 1030–1041. https://doi.org/10.1038/s41396-020-0590-x

Luther, G.W., Sundby, B., Lewis, B.L., Brendel, P.J., Silverberg, N., 1997. Interactions of manganese with the nitrogen cycle: Alternative pathways to dinitrogen. Geochimica et Cosmochimica Acta 61, 4043–4052. https://doi.org/10.1016/S0016-7037(97)00239-1

Ma, M., Overvest, P., Hijlkema, A., Mangold, S., McCammon, C., Voegelin, A., Behrends, T., 2023. Phosphate burial in aquatic sediments: Rates and mechanisms of vivianite formation from mackinawite. Chemical Engineering Journal Advances 16, 100565. https://doi.org/10.1016/j.ceja.2023.100565

März, C., Poulton, S.W., Beckmann, B., Küster, K., Wagner, T., Kasten, S., 2008. Redox sensitivity of P cycling during marine black shale formation: Dynamics of sulfidic and anoxic, non-sulfidic bottom waters. Geochimica et Cosmochimica Acta 72, 3703–3717. https://doi.org/10.1016/j.gca.2008.04.025

Mehner, T., 2009. Encyclopedia of inland waters. Academic Press.

Metzger, E., Maillet, G.M., 2021. REBELRED cruise,Thalia R/V. https://doi.org/10.17600/18001620

Metzger, E., Simonucci, C., Viollier, E., Sarazin, G., Prévot, F., Jézéquel, D., 2007. Benthic response to shellfish farming in Thau lagoon: Pore water signature. Estuarine, Coastal

769 and Shelf Science, Biogeochemical and contaminant cycling in sediments from a human-
770 impacted coastal lagoon 72, 406–419. https://doi.org/10.1016/j.ecss.2006.11.011
771 Migniot, C., 1993. Bilan de l'hydrologie et de l'hydrosédimentaire de l'estuaire de la Loire
772 au cours des deux dernières décénnies. Association pour la Protection de l'Environnement de
773 l'Estuaire de la Loire, Port Autonome de Nantes-St Nazaire, Nantes.
774 Migniot, C., 1972. L'évolution de la Gironde au cours de temps.
775 Morris, A.W., Bale, A.J., Howland, R.J.M., 1982. The dynamics of estuarine manganese
776 cycling. Estuarine, Coastal and Shelf Science 14, 175–192. https://doi.org/10.1016/S0302-
777 3524(82)80044-3
778 Mouret, A., Anschutz, P., Lecroart, P., Chaillou, G., Hyacinthe, C., Deborde, J., Jorissen,
779 F.J., Deflandre, B., Schmidt, S., Jouanneau, J.-M., 2009. Benthic geochemistry of manganese
780 in the Bay of Biscay, and sediment mass accumulation rate. Geo-Mar Lett 29, 133–149.
781 https://doi.org/10.1007/s00367-008-0130-6
782 Mucci, A., Boudreau, B., Guignard, C., 2003. Diagenetic mobility of trace elements in
783 sediments covered by a flash flood deposit: Mn, Fe and As. Applied Geochemistry 18, 1011–
784 1026. https://doi.org/10.1016/S0883-2927(02)00207-X
785 Mucci, A., Edenborn, H.M., 1992. Influence of an organic-poor landslide deposit on the
786 early diagenesis of iron and manganese in a coastal marine sediment. Geochimica et
787 Cosmochimica Acta 56, 3909–3921. https://doi.org/10.1016/0016-7037(92)90005-4
788 Nmor, S.I., Viollier, E., Pastor, L., Lansard, B., Rabouille, C., Soetaert, K., 2022. FESDIA
789 (v1.0): exploring temporal variations of sediment biogeochemistry under the influence of
790 flood events using numerical modelling. Geoscientific Model Development 15, 7325–7351.
791 https://doi.org/10.5194/gmd-15-7325-2022
792 OFB, 2017. . Le portail technique de l'OFB. URL https://professionnels.ofb.fr/fr/node/558
793 (accessed 3.1.24).
794 Oldham, V.E., Siebecker, M.G., Jones, M.R., Mucci, A., Tebo, B.M., Luther, G.W., 2019.
795 The Speciation and Mobility of Mn and Fe in Estuarine Sediments. Aquat Geochem 25, 3–26.
796 https://doi.org/10.1007/s10498-019-09351-0
797 Pant, H. k., Reddy, K. r., 2001. Phosphorus Sorption Characteristics of Estuarine
798 Sediments under Different Redox Conditions. Journal of Environmental Quality 30, 1474–
799 1480. https://doi.org/10.2134/jeq2001.3041474x
800 Pastor, L., Rabouille, C., Metzger, E., Thibault de Chanvalon, A., Viollier, E., Deflandre,
801 B., 2018. Transient early diagenetic processes in Rhône prodelta sediments revealed in

802 contrasting flood events. Continental Shelf Research 166, 65–76.
803 https://doi.org/10.1016/j.csr.2018.07.005
804 Perillo, Gerardo M. E., 1995. Chapter 2 Definitions and Geomorphologic Classifications of
805 Estuaries, in: Perillo, G. M. E. (Ed.), Developments in Sedimentology, Geomorphology and
806 Sedimentology of Estuaries. Elsevier, pp. 17–47. https://doi.org/10.1016/S0070-
807 4571(05)80022-6
808 Phillips, E.J.P., Lovley, D.R., 1987. Determination of Fe(III) and Fe(II) in Oxalate Extracts
809 of Sediment. Soil Science Society of America Journal 51, 938–941.
810 https://doi.org/10.2136/sssaj1987.03615995005100040021x
811 Postma, H., 1967. Sediment transport and sedimentation in the estuarine environment.
812 American Association of Advanced Sciences 83, 158–179.
813 Poulton, S.W., Canfield, D.E., 2005. Development of a sequential extraction procedure for
814 iron: implications for iron partitioning in continentally derived particulates. Chemical
815 Geology 214, 209–221. https://doi.org/10.1016/j.chemgeo.2004.09.003
816 Raiswell, R., Vu, H.P., Brinza, L., Benning, L.G., 2010. The determination of labile Fe in
817 ferrihydrite by ascorbic acid extraction: Methodology, dissolution kinetics and loss of
818 solubility with age and de-watering. Chemical Geology 278, 70–79.
819 https://doi.org/10.1016/j.chemgeo.2010.09.002
820 Raven, J.A., 1990. Predictions of Mn and Fe use efficiencies of phototrophic growth as a
821 function of light availability for growth and of C assimilation pathway. New Phytologist 116,
822 1–18. https://doi.org/10.1111/j.1469-8137.1990.tb00505.x
823 Rennert, T., Dietel, J., Heilek, S., Dohrmann, R., Mansfeldt, T., 2021. Assessing poorly
824 crystalline and mineral-organic species by extracting Al, Fe, Mn, and Si using (citrate-)
825 ascorbate and oxalate. Geoderma 397, 115095.
826 https://doi.org/10.1016/j.geoderma.2021.115095
827 Rickard, D., W.Luther, G., 2007. Chemistry of Iron Sulfides | Chemical Reviews [WWW
828 Document]. URL https://pubs.acs.org/doi/full/10.1021/cr0503658 (accessed 3.20.24).
829 Rothe, M., Kleeberg, A., Grüneberg, B., Friese, K., Pérez-Mayo, M., Hupfer, M., 2015.
830 Sedimentary Sulphur:Iron Ratio Indicates Vivianite Occurrence: A Study from Two
831 Contrasting Freshwater Systems. PLOS ONE 10, e0143737.
832 https://doi.org/10.1371/journal.pone.0143737
833 Rozan, T.F., Taillefert, M., Trouwborst, R.E., Glazer, B.T., Ma, S., Herszage, J., Valdes,
834 L.M., Price, K.S., Luther III, G.W., 2002. Iron-sulfur-phosphorus cycling in the sediments of
835 a shallow coastal bay: Implications for sediment nutrient release and benthic macroalgal

836 blooms. Limnology and Oceanography 47, 1346–1354.
837 https://doi.org/10.4319/lo.2002.47.5.1346
838 Sanchez-Cabeza, J.A., Ruiz-Fernández, A.C., 2012. 210Pb sediment radiochronology: An
839 integrated formulation and classification of dating models. Geochimica et Cosmochimica
840 Acta, Environmental Records of Anthropogenic Impacts 82, 183–200.
841 https://doi.org/10.1016/j.gca.2010.12.024
842 Saulnier, I., Mucci, A., 2000. Trace metal remobilization following the resuspension of
843 estuarine sediments: Saguenay Fjord, Canada. Applied Geochemistry 15, 191–210.
844 https://doi.org/10.1016/S0883-2927(99)00034-7
845 Schmidt, S., Howa, H., Diallo, A., Martín, J., Cremer, M., Duros, P., Fontanier, C.,
846 Deflandre, B., Metzger, E., Mulder, T., 2014. Recent sediment transport and deposition in the
847 Cap-Ferret Canyon, South-East margin of Bay of Biscay. Deep Sea Research Part II: Topical
848 Studies in Oceanography, Submarine Canyons: Complex Deep-Sea Environments Unravelled
849 by Multidisciplinary Research 104, 134–144. https://doi.org/10.1016/j.dsr2.2013.06.004
850 Scholz, F., McManus, J., Mix, A.C., Hensen, C., Schneider, R.R., 2014. The impact of
851 ocean deoxygenation on iron release from continental margin sediments. Nature Geosci 7,
852 433–437. https://doi.org/10.1038/ngeo2162
853 Shaw, T.J., Gieskes, J.M., Jahnke, R.A., 1990. Early diagenesis in differing depositional
854 environments: The response of transition metals in pore water. Geochimica et Cosmochimica
855 Acta 54, 1233–1246. https://doi.org/10.1016/0016-7037(90)90149-F
856 Sivan, O., Alder, M., Pearson, A., Gelman, F., Bar-or, I., G.John, S., Eckert, W., 2011.
857 Geochemical evidence for iron- mediated anaerobic oxidation of methane [WWW
858 Document]. URL
859 https://aslopubs.onlinelibrary.wiley.com/doi/epdf/10.4319/lo.2011.56.4.1536 (accessed
860 3.20.24).
861 Slomp, C.P., Mort, H.P., Jilbert, T., Reed, D.C., Gustafsson, B.G., Wolthers, M., 2013.
862 Coupled Dynamics of Iron and Phosphorus in Sediments of an Oligotrophic Coastal Basin
863 and the Impact of Anaerobic Oxidation of Methane. PLOS ONE 8, e62386.
864 https://doi.org/10.1371/journal.pone.0062386
865 Sundby, B., 2006. Transient state diagenesis in continental margin muds. Marine
866 Chemistry, 8th International Estuarine Biogeochemistry Symposium - Introduction 102, 2–12.
867 https://doi.org/10.1016/j.marchem.2005.09.016
868 SYVEL, 2021. . GIPLE : Mesures Automatisées en Réseau pour l'Environnement Littoral.
869 URL https://www.loire-estuaire.org/dif/do/network (accessed 3.20.24).

Thamdrup, B., Dalsgaard, T., 2000. The fate of ammonium in anoxic manganese oxide-rich marine sediment. Geochimica et Cosmochimica Acta 64, 4157–4164. https://doi.org/10.1016/S0016-7037(00)00496-8

Thibault De Chanvalon, A., Metzger, E., Mouret, A., Knoery, J., Chiffoleau, J.-F., Brach-Papa, C., 2016. Particles transformation in estuaries: Fe, Mn and REE signatures through the Loire Estuary. Journal of Sea Research 118, 103–112. https://doi.org/10.1016/j.seares.2016.11.004

Thibault de Chanvalon, A., Metzger, E., Mouret, A., Knoery, J., Geslin, E., Meysman, F.J.R., 2017. Two dimensional mapping of iron release in marine sediments at submillimetre scale. Marine Chemistry 191, 34–49. https://doi.org/10.1016/j.marchem.2016.04.003

Thibault de Chanvalon, A., Mouret, A., Knoery, J., Geslin, E., Péron, O., Metzger, E., 2016. Manganese, iron and phosphorus cycling in an estuarine mudflat, Loire, France. Journal of Sea Research, Recent and past sedimentary, biogeochemical and benthic ecosystem evolution of the Loire Estuary (Western France) 118, 92–102. https://doi.org/10.1016/j.seares.2016.10.004

Vandieken, V., Nickel, M., Jørgensen, B.B., 2006. Carbon mineralization in Arctic sediments northeast of Svalbard: Mn(IV) and Fe(III) reduction as principal anaerobic respiratory pathways. Marine Ecology Progress Series 322, 15–27. https://doi.org/10.3354/meps322015

Widerlund, A., Ingri, J., 1996. Redox cycling of iron and manganese in sediments of the Kalix River estuary, Northern Sweden. Aquat Geochem 2, 185–201. https://doi.org/10.1007/BF00121631

Woodruff, J.D., Geyer, W.R., Sommerfield, C.K., Driscoll, N.W., 2001. Seasonal variation of sediment deposition in the Hudson River estuary. Marine Geology 179, 105–119. https://doi.org/10.1016/S0025-3227(01)00182-7

Xiong, Y., Guilbaud, R., Peacock, C.L., Cox, R.P., Canfield, D.E., Krom, M.D., Poulton, S.W., 2019. Phosphorus cycling in Lake Cadagno, Switzerland: A low sulfate euxinic ocean analogue. Geochimica et Cosmochimica Acta 251, 116–135. https://doi.org/10.1016/j.gca.2019.02.011

Yu, C., Virtasalo, J.J., Karlsson, T., Peltola, P., Österholm, P., Burton, E.D., Arppe, L., Hogmalm, J.K., Ojala, A.E.K., Åström, M.E., 2015. Iron behavior in a northern estuary: Large pools of non-sulfidized Fe(II) associated with organic matter. Chemical Geology 413, 73–85. https://doi.org/10.1016/j.chemgeo.2015.08.013